The influence of zirconium content on the microstructure, mechanical properties, and biocompatibility of in-situ alloying Ti-Nb-Ta based β alloys processed by selective laser melting

Kong, Weihuan; Cox, Sophie C.; Lu, Yu; Villapun, Victor; Xiao, Xiaoling; Ma, Wenyou; Liu, Min; Attallah, Moataz M.

DOI:
10.1016/j.msec.2021.112486

Document Version
Peer reviewed version

Citation for published version (Harvard):
Kong, W, Cox, SC, Lu, Y, Villapun, V, Xiao, X, Ma, W, Liu, M & Attallah, MM 2021, 'The influence of zirconium content on the microstructure, mechanical properties, and biocompatibility of in-situ alloying Ti-Nb-Ta based β alloys processed by selective laser melting', *Materials Science and Engineering C*, vol. 131, 112486. https://doi.org/10.1016/j.msec.2021.112486

The Influence of Zirconium Content on the Microstructure, Mechanical properties, and Biocompatibility of *in-situ* Alloying Ti-Nb-Ta Based *β* Alloys Processed by Selective Laser Melting

Weihuan Kong [1] , Sophie C. Cox[2], Yu Lu [1], Victor Villapun [2], , Xiaoling Xiao [3], Wenyou Ma [4], Min Liu [4]*, Moataz M. Attallah [1]*

1. School of Materials and Metallurgy, University of Birmingham, Edgbaston, B15 2TT, UK

2. School of Chemical Engineering, University of Birmingham, Edgbaston, B15 2TT, UK

3. Guangdong Institute of Analysis, Guangzhou, 510651, PR China

4. National Engineering Laboratory for Modern Materials Surface Engineering Technology, The Key Lab of Guangdong for Modern Surface Engineering Technology, Guangdong Institute of New Materials, Guangzhou, 510651, PR China

*Correspondence:

Min Liu: liumin@gdas.gd.cn

Moataz M. Attallah: m.m.attallah@bham.ac.uk

Abstract

This study investigates Ti-Nb-Ta based *β* alloys with different zirconium additions (0, 5, 9 wt. %) manufactured by SLM. A low level of as-fabricated defects is obtained: the relative density of TNT(Z) alloys is >99.97% with the keyhole size in a range of 3—20 μm. BF TEM images combining SAD patterns of TNT(Z) alloys show single *β* phase obtained inside the beta matrix; BF-STEM images reveal potential nano-scale grain boundary alpha phase precipitation. Zirconium functions as a neutral element in these high *β*-stabilized Ti-Nb-Ta based alloys. An increase in Vickers hardness and UTS caused by zirconium additions is observed, which is explained by beta grain refinement because higher degree of undercooling occurs. Corrosion ions of TNT(Z) alloys released from immersion testing at each time intervals show extremely small concentrations (<10 μg/L). It indicated that good biocompatibility during culture with the negligible corrosion ions. High strength-to-modulus ratio *β* Ti alloys together with excellent biological response show their prospect for biomedical applications.

Keywords: *In-situ* alloying, Ti-Nb-Ta based β alloys, Zirconium addition, Equiaxed microstructure, Strength-to-modulus ratio, Static immersion testing

1. Introduction

Osteoarthritis is the most common degenerative human joint disease worldwide, and is characterized by the loss of joint cartilage leading to pain, and even loss of load-bearing function. It mainly occurs in the aged population, affecting 9.6% of men and 18% of women aged >60 years [1]. Traditionally, the end-stage pain cannot be removed by conservative modalities, like intra-articular injections, necessitating joint replacement surgery [2]. Among attractive candidate materials for total hip replacement (THR) and total knee replacement (TKR), metallic orthopedic implants play a predominant role mainly due to their mechanical stability [3]. As Ti-6Al-4V alloy has attractive mechanical properties and corrosion resistance, as well as good biocompatibility, it becomes a preferred material for load-bearing implant manufacturing to date [4]. However, there are still some doubts as to its functional reliability as a bimodal (α+β) alloy with a Young's modulus range of 100-120 GPa [5], which is much higher than that of cortical bone (10-30 GPa) [6]. Therefore, the "stress shielding" effect occurs after artificial prosthesis instalment in the long term. It is considered as a stiffer implant sustains the main load from the human body and causes a reduction in the stress level within bone, which leads to the detrimental remodeling of peri-prosthetic bone, thus the implant surrounding tissue resorption happens due to the change in the load transfer after total joint replacement (TJR) surgery [7–10]. Therefore, many researchers are investigating low-modulus Ti-6Al-4V lattice structure implants by additive manufacturing [11–13]. But a question mark surrounds their poor fatigue lifetime after subsequent artificial joint replacement. Another concern is that the metallic wear debris and *in vivo* corrosion products with vanadium may release potential cytotoxicity [4,14].

Beta titanium alloys can be described as any Ti alloys with the addition of enough beta stabilizers to retain up to 100% beta phase at room temperature upon cooling from above beta transus temperature [15]. Titanium alloys, combined with human-friendly β stabilizers such as niobium, molybdenum, and tantalum have been investigated for low-modulus biomechan-

ical material applications [16–19]. Using the DV-Xα cluster method [20], Abdel-Hady et al. [21] reported that Ti-29Nb-13Ta-4.6Zr alloy (approx. 2.88 $\overline{Bo}$ and 2.46 $\overline{Md}$) was measured with low elastic modulus at around 50 GPa. Based on molecular orbital calculation, $\overline{Bo}$ (average covalent bond strength between Ti and other alloying elements) and $\overline{Md}$ (average *d*-orbital energy level of the involved alloying elements) are used to predict mechanical properties of the specific Ti alloys. Most existing studies have focused on traditional processing, and mechanical properties of β Ti alloys. Among them, Sakaguchi et al. [22] investigated metastable as-forged and solution-treated Ti-Nb-Ta-Zr-O alloys with different niobium additions (20, 25, 30, 35 wt. %), demonstrating that all aforementioned alloys obtained ultimate tensile strength (UTS) of more than 700 MPa, and some of them possessed good elongation (more than 20%) with low Young's modulus. Besides that, Zhukova et al. [23] compared the electrochemical behavior of Ti-22Nb-6Ta (at.%) with commercially pure (CP) titanium in simulated physiological medium (Hank's solution), reporting that the Ti-Nb-Ta β alloy possesses higher open circuit potential (OCP) values under cycling conditions. They also found that the oxide film exhibits superior resistance to the applied cyclic load when compared to CP titanium. Gordin et al. [24] and Neacsu et al. [25] reported short-term *in vitro* M3CT3-E1 preosteoblast results based on traditional manufactured Ti-Nb-X β alloys. They found that the investigated β Ti alloys seemingly obtain equal or even better performance than CP titanium during different types of cell-relevant assays (cytotoxicity, differentiation, etc.).

Metal additive manufacturing (AM) is based on the principle of incremental layer-by-layer material consolidation, facilitating the fabrication of complicated components through the controlled melting or sintering of feedstock materials with the aid of energy sources, e.g. lasers, electron beams, etc. [26–28]. Considering factors such as less feedstock consumption in manufacturing components, supply chain and assembly line simplification, customized complex-part fabrication, metal AM process is an attractive option for manufacturing high-end products when compared to traditional manufacturing techniques [29–31]. Among varieties of additive manufacturing techniques, powder bed fusion (PBF) techniques are typically suitable for manufacturing delicate, custom biomedical implants with high dimensional accuracy [32–35].

A limited amount of research on additive manufacturing β Ti alloys exists to date. Zhang et al. [36] and Liu et al. [37] investigated microstructure and mechanical properties of Ti-24Nb-4Zr-8Sn dense and lattice samples based on electron beam melting (EBM) and selective laser melting (SLM). Their studies illustrated keyhole defect (and its formation mechanism), which is caused by in-process tin vaporization because tin has the lowest boiling point among the evolved alloying elements. However, there does not appear to have publications which specifically demonstrate microstructure evolution of Ti-Nb-Ta-Zr alloys undergoing fast heating & cooling rates, and laser re-melting via PBF. The function of so-called neutral element Zr [38] on β phase stability is not confirmed in the aforementioned thermal history, and there is still some dispute about the function of Zr in Ti-Nb based β alloys manufactured by traditional manufacturing techniques. Hao et al. [39] mentioned the combined alloying addition of Zr and Sn is effective in raising the beta transus temperatures of Ti–Nb based alloys, thus potentially narrowing beta phase region. Abdel-Hady et al. [21] concludes that zirconium works as a β stabilizing element in Ti-Zr-Nb β alloys over the wide range of Zr content in solution-treated and aged conditions. The present study investigates *in-situ* alloying Ti-Nb-Ta based β alloys with different zirconium additions (0, 5, 9 wt. %) manufactured by SLM. The as-fabricated parameter optimization, microstructure evolution and process-induced defects distribution, tensile testing performance, ion release evaluation, and M3CT3-E1 preosteoblast cell viability of TNT(Z) alloys are sequentially characterized. We also introduce solution treatment followed by water quenching aiming to reduce their Young's moduli, which is the starting point of decreasing the "stress shielding" effect based on its load-bearing application.

2. Materials and Methods

2.1 Powder feedstock preparation

Pure element powder was chosen for as-designed materials powder mixing. The chemical composition of the three designed TNT(Z) alloys in this work (given in Table 1) are Ti-34Nb-13Ta, Ti-34Nb-13Ta-5Zr, Ti-34Nb-13Ta-9Zr, hereafter termed TNT, TNT5Zr and TNT9Zr

Table 1 As designed chemical composition of the three employed alloys (wt. %).

	TNT	TNT5Zr	TNT9Zr
Ti	Balance	Balance	Balance
Nb	34	34	34
Ta	13	13	13
Zr	0	5	9

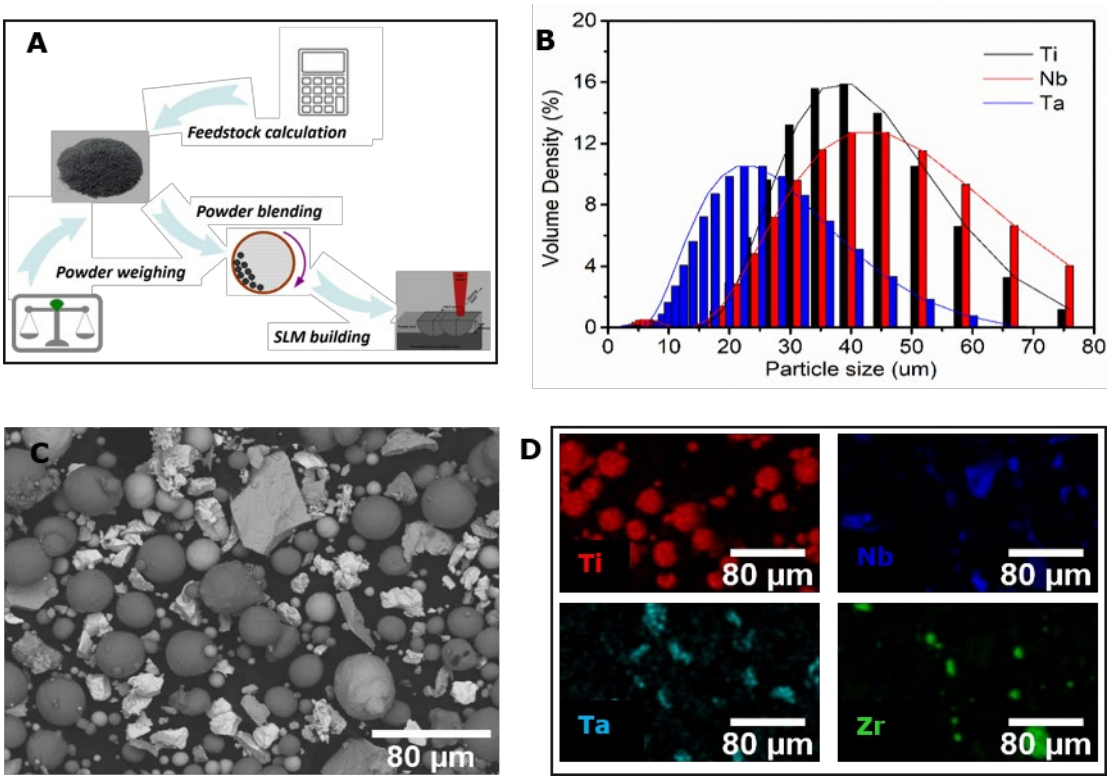

Fig. 1. (A) Schematic of the as-SLMed TNT(Z) alloys manufactured by *in-situ* alloying. Characteristic of feedstock powder**:** (B) particle size distribution (PSD) of as-received pure Ti, Nb, Ta powder, (C) particle morphology of blended TNT9Zr (e.g.) powder, and (D) EDS map of the involved alloying elements. Note: the SLM process figure in Fig. 1A is sourced from article [40]. PSD of Zr powder is not listed as it is too reactive to be measured.

alloy, respectively. Spherical Ti, Zr powder (TLS, Germany) with nominal particle size distribution (15—83 μm) and (10—45 μm) were gas atomized in argon atmosphere. Rocky Nb (Elite, UK), Ta powder (H.C. Starck, Germany) with an average particle size (D_{50}) of 43.9 μm

and 23.4 μm (Fig. 1B) was manufactured through a hydride-dehydride process. Powder weighing was finished in a glove box with an argon protective atmosphere. Following that, powder blending was performed for ten hours in a horizontal rotating drum, as-seen in Fig. 1A. The blended powder was characterized by energy-dispersive X-ray spectroscopy (EDS, Bruker) mapping, aiming to check blending performance before the SLM manufacturing process (Fig. 1C-D).

2.2 Selective laser melting

An M2 Cusing SLM system (Concept Laser, GE Additive) was adopted to fabricate TNT, TNT5Zr and TNT9Zr samples on Ti alloy substrate. The machine was equipped with a 400 W Yb:YAG fiber laser at a wavelength of 1064 nm. The laser beam spot size was focused at approx. 63 μm. Considering the high oxidation risk of these pure elements, high purity protective argon (99.8%) was continually pumped into the process chamber until the as-fabricated parts thoroughly cooled down. The key SLM parameters investigated for manufacturing parameter optimization were: laser power (240—300 W), scan speed (400—1000 mm/s), and scan spacing (35—65 μm). The chessboard scan strategy with scan vectors rotated by 90º in adjacent 5 x 5 mm blocks was used for building parts, and each successive layer was shifted by 1 mm in both the X and Y directions; the preset layer thickness was 20 μm. Based on SEM (TM3000, Hitachi) backscattered electron (BSE) images (nine low Mag. images for each parameter), area fraction of porosity, and un-melted Nb and Ta content through image processing software (Image J, Fiji), were analyzed. All data were recorded as the mean ± standard deviation (SD). The manufactured parts were 7 x 7 x 7 mm cubes and sub-size dog-bone tensile specimens with 75 mm total length. The sub-size tensile specimen dimension was designed according to the ASTM- E8/ E8M-13a standard [41]. The tailored cross-section parts were horizontally manufactured with a height of 10 mm, then sliced into 1.5 mm thickness dog-bone test-pieces (Fig. 2) using wire electron discharge machining (EDM, GF Machining Solutions).

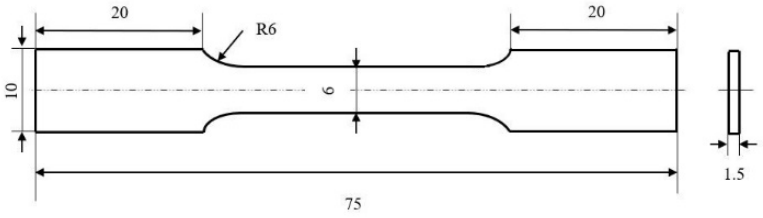

Fig. 2. Specimen geometry of dog-bone tensile test specimen in mm.

2.3 Microstructure and micro-defects characterization

Metallographic specimens were prepared using automatic grinding and polishing equipment (Tegramin 30, Struers), and then etched by Kroll's reagent (2% HF + 6% HNO_3 + 92% H_2O). The phase identification was performed by X-ray diffractometer (XRD) (AXRD, Proto) with Cu Kα radiation, and XRD spectra were collected by a fixed parameter of 0.02° step size and a 2s time/step. Electron backscatter diffraction (EBSD) mapping of samples were observed with a field-emission gun (FEG) SEM (NNS450, FEI) equipped with EBSD detector (EDAX, Ametek). The selected step size was 0.8 μm, aiming to maintain high EBSD indexing rate. A transmission electron microscope (2100, JEOL) operating at 200 kV was used to capture bright-field (BF) images and selected area diffraction (SAD) pattern, bright-field scanning transmission electron microscopy (BF-STEM) images. Thin foils for TEM were prepared through an argon ion milling technique (Gatan PIPS, Ametek), involving gradient milling by different Ar ion energy and sputter angle settings. The porosity and un-melted particles of cylinder specimens (D1.6 H7.5) were analyzed with micro-CT (Skyscan, Bruker). The scan parameters were an accelerating voltage of 165 kV and a current of 75 μA for a 360º scan. A total of 2,500 projections were collected on a charge-coupled device (CCD) detector using a 1s exposure time. The data was reconstructed and visualized using Nikon Pro 3D and Avizo software, respectively.

2.4 Differential scanning calorimetry and solution treatment

Differential scanning calorimetry (DSC) analysis was performed by heat-flux DSC cell

(404 F1 Pegasus, Netzsch). As-fabricated TNT(Z) samples (approx. 20 mg each sample) were separately loaded in recrystallized alumina crucible, sealed with a lid using the same material. It ran with a constant heating and cooling rate of 10℃/min in argon atmosphere to predict the thermodynamic properties. The heating temperature was increased to a maximum temperature (1200℃), then cooled down to identify phase transformation characteristics of each alloy. Solution treatment specimens were encapsulated in evacuated quartz tubes, dwelled at 750℃ in an electric furnace for one hour, followed by quenching into water.

2.5 Micro-hardness and mechanical properties

Mirror-like specimens were mounted on a micro-hardness tester (Wilson VH1202, Buehler) for Vickers hardness measurement. The test for each sample was performed with a 100g load and 10 times linearly, indented with recommended spacing according to the ASTM E384-17 standard [42]. The as-fabricated specimens in tensile testing were carried out perpendicularly build direction at room temperature. The stress-strain curves were measured at a crosshead speed of 0.5 mm/min at room temperature using a tensile testing machine (2500, Zwick/Roell). Two specimens per alloy were tested in order to average tensile properties, and a clip-on extensometer was attached to the 15 mm gage length of specimen until rupture, then fracture morphology was observed using a SEM (NNS450, FEI).

2.6 Metallic ion release evaluation and cell viability

As-fabricated Ti-Nb-Ta based metallic samples (two-side polished, 10 x 10 mm) were ultrasonically cleaned in pure ethanol for 10 minutes and then sterilized in autoclave for 90 minutes. For the ion release study, one sample per each metallic material was submerged for 7 days, 14 days, 21 days, 30 days, 90 days, and 180 days in 20 mL of minimal essential medium (MEM) supplemented with 1% penicillin/streptomycin, and 0.5 g/L L-glutamine. Meanwhile, the control group for each time interval contained 20 mL aforementioned MEM containing medium without any metallic sample. These liquid samples were all kept in a cell incubator with 5% CO_2 at 37 °C atmosphere. From these 20 mL after-immersion mediums, the 15 mL

was used for metallic ion release evaluation, and the other 5 mL was a part of cell culture medium to perform MC3T3-E1 cell viability assays. The measurement of ion release after the immersion test was performed using inductively coupled plasma optical emission spectrometry (ICP-OES) (Optima 8000, PerkinElmer). Before the measurement of metallic ions in all samples, the calibration of standardized samples was conducted with the involved elements at a wavelength of Ti (334.940 nm), Nb (309.418 nm), Ta (226.230 nm), and Zr (343.823 nm). The correlate coefficients of these four calibrations were $\geqslant 0.999$. Two runs measurements were set up to demonstrate these element analysis results. After the longest time interval (180 days) immersion test, MC3T3-E1 preosteoblast was seeded and cultured in a flask with standard culture medium. The after cultured MC3T3-E1 cells were detached from the bottom surface of the flask using 0.25% trypsin-EDTA solution (5 minutes at 37℃), then seeded in each well (24-well plate) at a concentration of 2×10^4 cells/cm^2. The medium for cell culture was 0.5 mL medium after the immersion test, supplemented with 0.5 mL standard culture medium including serum (MEM, 10% fetal bovine serum, 1% penicillin/streptomycin, and 0.5g/L L-glutamine); alongside a control group containing standard supplemented medium was set up. The plate was then kept in the cell incubator for 24 hours. Alamar blue assay [43] in 96-well plate was performed using a spectrophotometer (Spark, Tecan) at a wavelength of 560 nm excitation and 590 nm emission. This assay was conducted in triplicate. The viability of cells after-immersion medium was analyzed by staining with calcein-AM and propidium iondide. Stained cells were visualized using a microscope imaging system (EVOS M5000, Thermo Scientific). Analysis of Variance (ANOVA) and two-tailed t-tests were performed for Alamar blue results, with a p value <0.05 considered as being statistically significant.

3. Results

3.1 Selective laser melting parameter optimization

The relationship between un-melted particles, porosity and PBF key parameters, is presented in Fig. 3A-C. Fig. 3A shows a clear tendency: the percentage of un-melted Nb

decreases to a large extent from 4.55% to 1.93% when laser power rises from 240 W to the maxima (300 W); the variances of Y-values (un-melted Nb, Ta also porosity) also become smaller when laser power increases. No ideal processing window obtained inside this parameter group after considering the best sample with relatively high value of porosity (2.2%) and un-melted Ta (0.7%). In Fig. 3B, the slow scan speed (500 mm/s) combining other preset parameters is considered an optional processing parameter with low defect level after conducting a batch of Y-values versus scan speed characterization. It also can be found the un-melted particles and porosity level is much higher in samples manufactured by high scan speed,

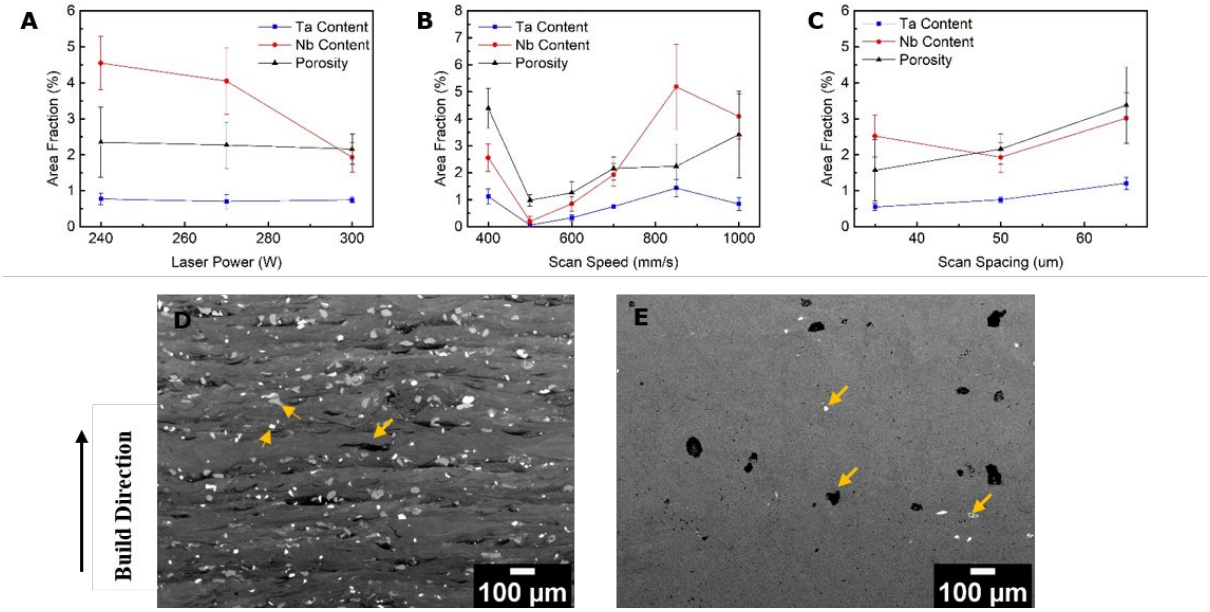

Fig. 3. (A) Un-melted Ta & Nb content and porosity versus laser power; the preset parameters are: 700 mm/s scan speed, 50 μm scan spacing. (B) Un-melted Ta & Nb content and porosity versus scan speed; the preset parameters are: 300 W laser power, 50 μm scan spacing. (C) Un-melted Ta & Nb content and porosity versus scan spacing; the preset parameters are: 300 W laser power, 700 mm/s scan speed. (D) Backscattered SEM image of as-built TNT specimen with low energy density, and (E) with high energy density. Note: arrows point out grey particle (Nb) and bright particle (Ta), and porosity features ((D) lack of fusion, (E) keyhole).

such as 850 mm/s, when compared to the counterpart manufactured by low scan speed (e.g. 500 mm/s). The consistent result has been found in Zhang et al. [36] work, the quality of parts fabricated by high scan speed is poor because the laser incident energy is insufficient to melt

the alloy with refractory elements. No obvious Y-values versus scan spacing fluctuation is found after increasing from 35 μm to 50 μm (Fig. 3C). It means that the defects level is not severely affected by scan spacing factor in the parameter arrays. Additionally, low energy density and high energy density as-built TNT specimen SEM (BSE) images are provided in Fig. 3D-E. The low energy density case could happen with a low laser power (e.g. 240 W) or high scan speed (e.g. 1000 mm/s); the porosity type is mainly a lack of fusion (arrows in Fig. 3D), and a high percentage of un-melted Nb & Ta disperses randomly during each layer manufacturing. The mechanism of lack of fusion voids has been concluded that inadequate penetration of molten pool from the upper layer into the previous layer [44,45]. On the other hand, the high energy density case could happen in a low scan speed (e.g. 500 mm/s); the main porosity formation is keyhole [37,46] (arrows in (Fig. 3E), and an extremely low percentage of un-melted Nb & Ta appears in the specimen matrix. The same defect characterization method was chosen for TNT5Zr and TNT9Zr alloy build parameter optimization by changing laser scan speed.

3.2 Phase analysis and microstructure

Fig. 4 shows the XRD profiles of as-fabricated TNT samples with different Zr additions. As seen, these samples all obtained main β phase with the highest intensity peak (110). The diffraction angles for $(110)_{\beta}$ atomic arrangement plane in TNT, TNT5Zr, TNT9Zr alloys are 38.70º, 38.53º, and 38.43º respectively. There is a low intensity suspicious alpha peak at around 35º of the three alloys. IPF maps of as-fabricated TNT alloy (Fig. 5A-B) show equiaxed and columnar grain formation, and micro-pores are randomly located in the material matrix. <001> fiber texture is observed by <001> IPF (Fig. 5C), and the phase distribution map (Fig. 5D) of TNT alloy indicates that beta phase matrix (red contrast) existence, and precipitates (green contrast) appear along grain boundary. The same type of grain formation and as-fabricated pore features are also observed in TNT5Zr (Fig. 6A-B) and TNT9Zr alloys (Fig. 7A-B). <001> fiber texture is kept in TNT alloys with zirconium additions, and the maximum texture indexes are between 1 and 3 (Fig. 6C & Fig. 7C). Additionally, Fig. 6D & Fig. 7D demonstrate phase distribution maps of TNT5Zr and TNT9Zr alloy with grain boundary precipitates. The grain

size (Fig. 8A) and misorientation angle (Fig. 8B) of the three alloys prove that TNT5Zr, TNT9Zr alloys possess a higher percentage of fine grain size (<30 μm) grains than the TNT sample. The high-angle grain boundary (greater than 15°) is the main tilt boundary of the three alloys after misorientation angle quantification analysis. On the nanoscopic scale, Fig. 9A shows a BF micrograph taken from the beta matrix of as-fabricated TNT alloy, together with a SAD pattern viewed along $[111]_{\beta}$ zone axis. It should be noted that no formation of metastable precipitates (e.g. ω or α'') inside beta matrix. Fig. 9B presents the BF-STEM image of as-fabricated TNT alloy, captured from a region close to grain boundary. It indicates the existence of nano-scale precipitates along the grain boundary. The BF image and SAD pattern obtained from the beta matrix of as-fabricated TNT5Zr alloy are presented in Fig. 9C, which shows no precipitation in the beta matrix. The BF-STEM image (Fig. 9D) indicates dispersive nano-scale precipitates occur at the grain boundary. Similarly, a single beta phase microstructure is observed in the BF image and its SAD pattern (Fig. 9E) of as-fabricated TNT9Zr alloy. Meanwhile, potential precipitation is found along beta grain boundary (Fig. 9F).

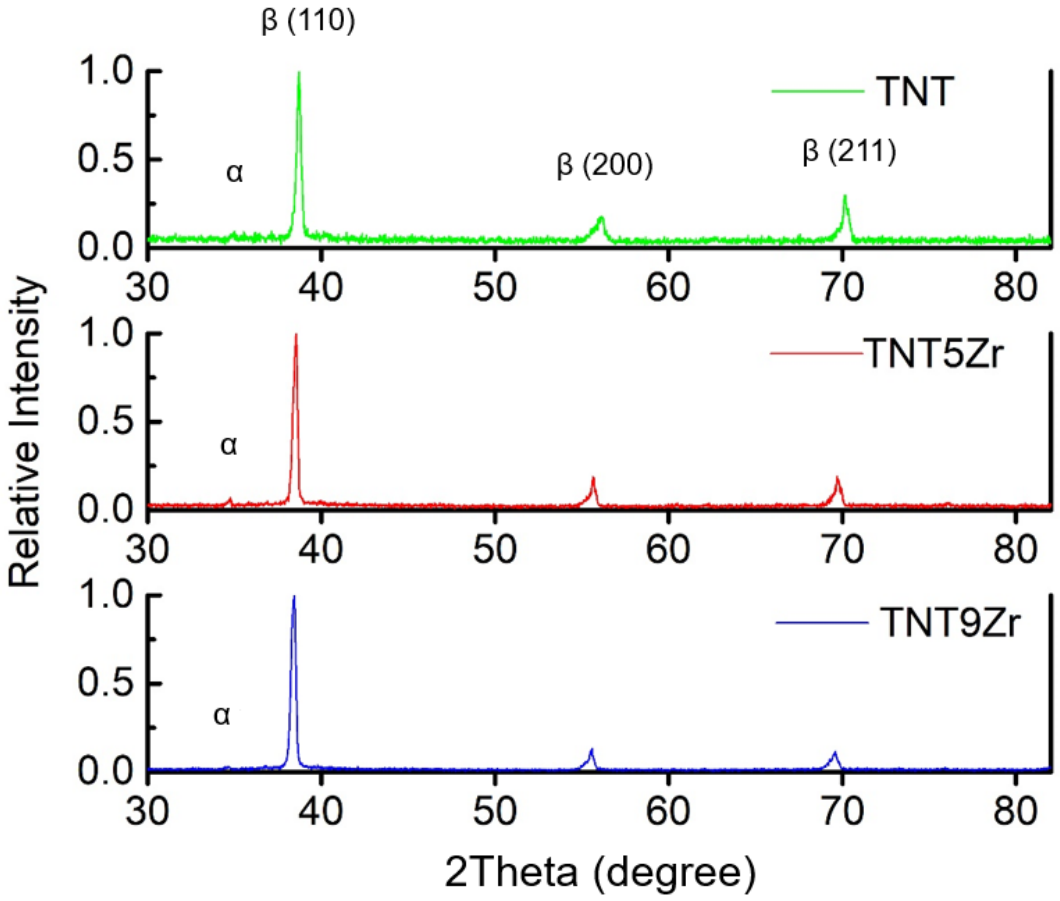

Fig. 4. X-ray diffraction patterns of as-fabricated TNT, TNT5Zr, TNT9Zr alloys.

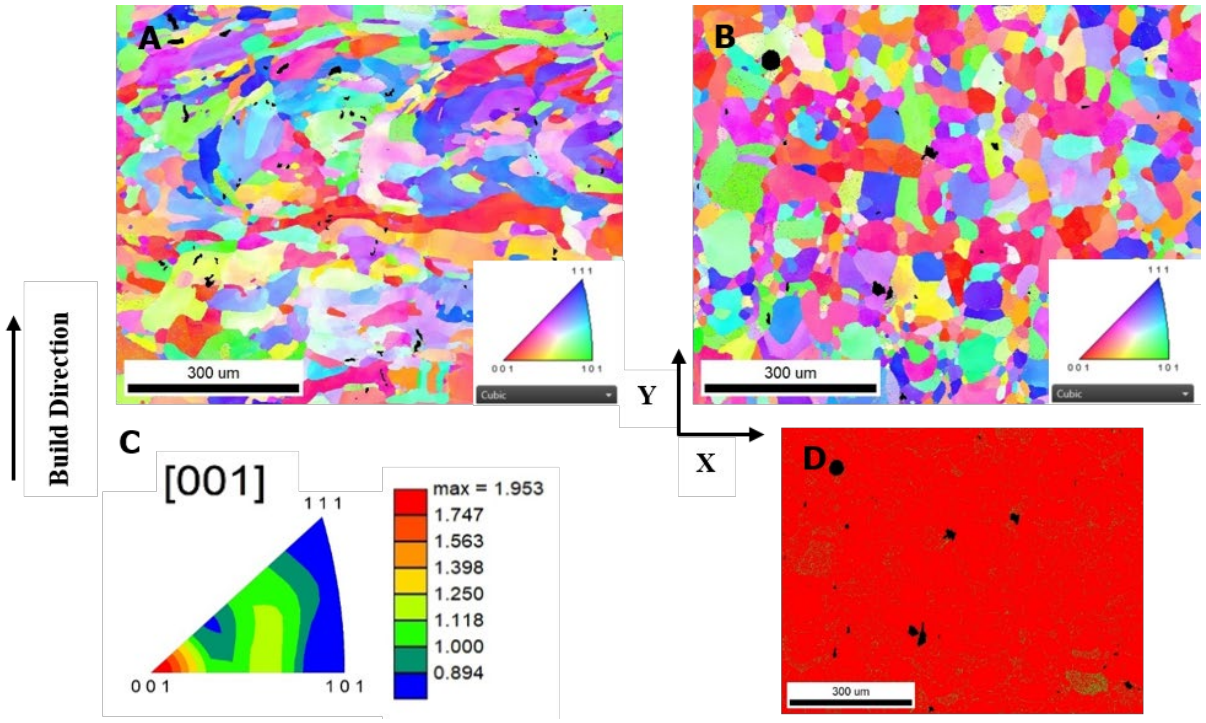

Fig. 5. EBSD results of SLM-processed TNT alloy: (A) auto inverse pole figure (IPF) map in parallel build

direction, (B) auto inverse pole figure (IPF) map in perpendicular build direction, (C) <001> inverse pole figure (IPF), and (D) phase distribution map. Note: red denotes beta Ti, green denotes precipitate phases.

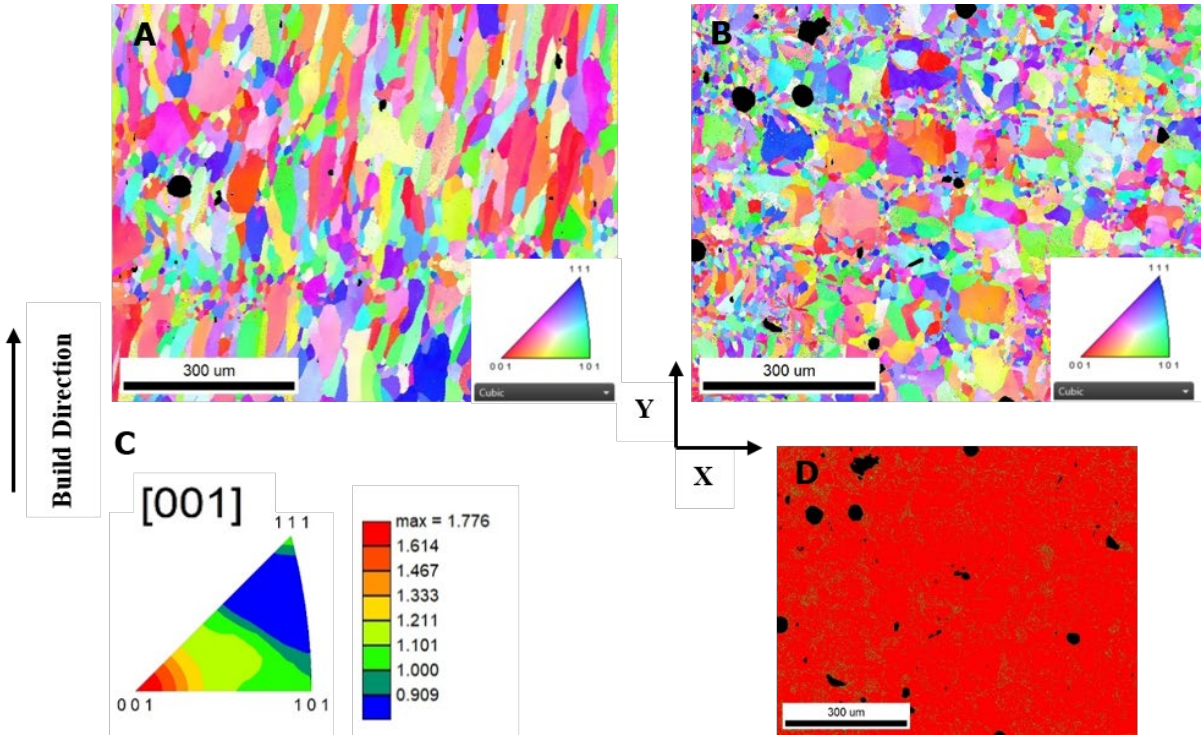

Fig. 6. EBSD results of SLM-processed TNT5Zr alloy: (A) auto inverse pole figure (IPF) map in parallel build direction, (B) auto inverse pole figure (IPF) map in perpendicular build direction, (C) <001> inverse pole figure (IPF), and (D) phase distribution map. Note: red denotes beta Ti, green denotes precipitate phases.

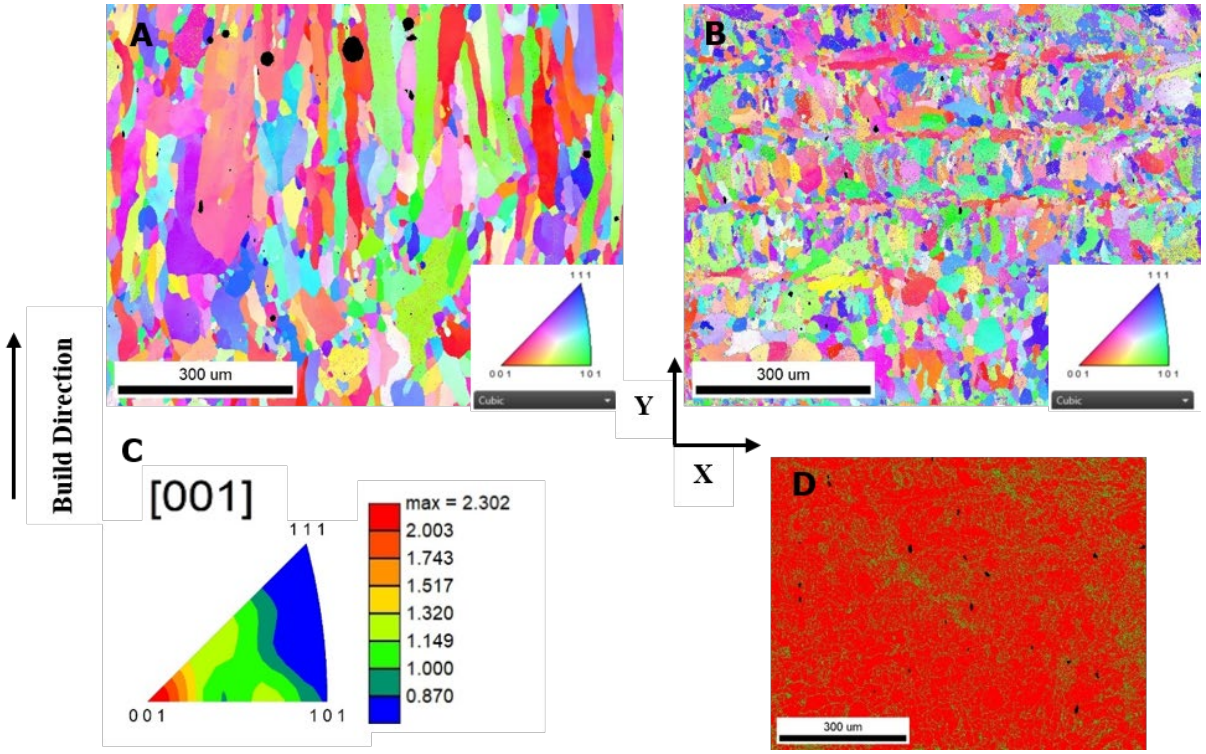

Fig. 7. EBSD results of SLM-processed TNT9Zr alloy: (A) auto inverse pole figure (IPF) map in parallel build direction, (B) auto inverse pole figure (IPF) map in perpendicular build direction, (C) <001> inverse pole figure (IPF), and (D) phase distribution map. Note: red denotes beta Ti, green denotes precipitate phases.

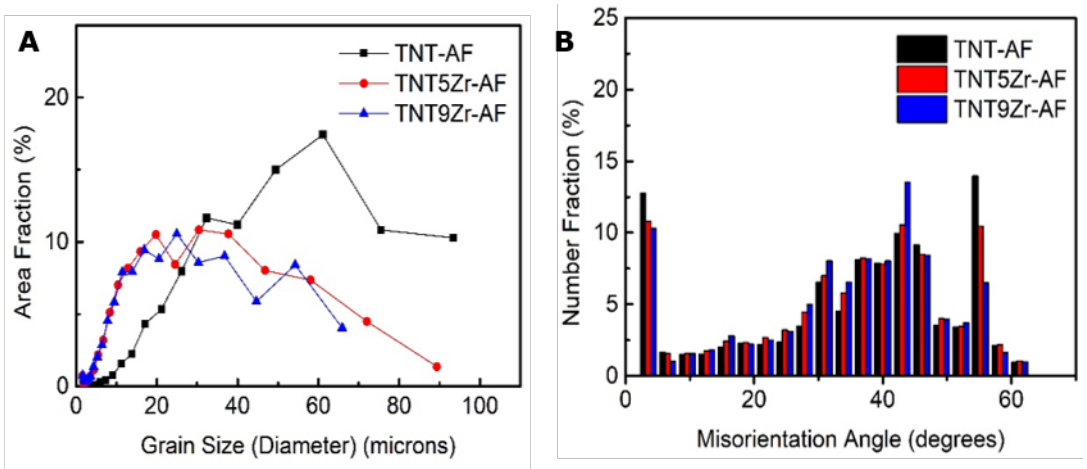

Fig. 8. EBSD quantitative results of SLM-processed TNT, TNT5Zr, TNT9Zr alloys: (A) grain size and (B) misorientation angle.

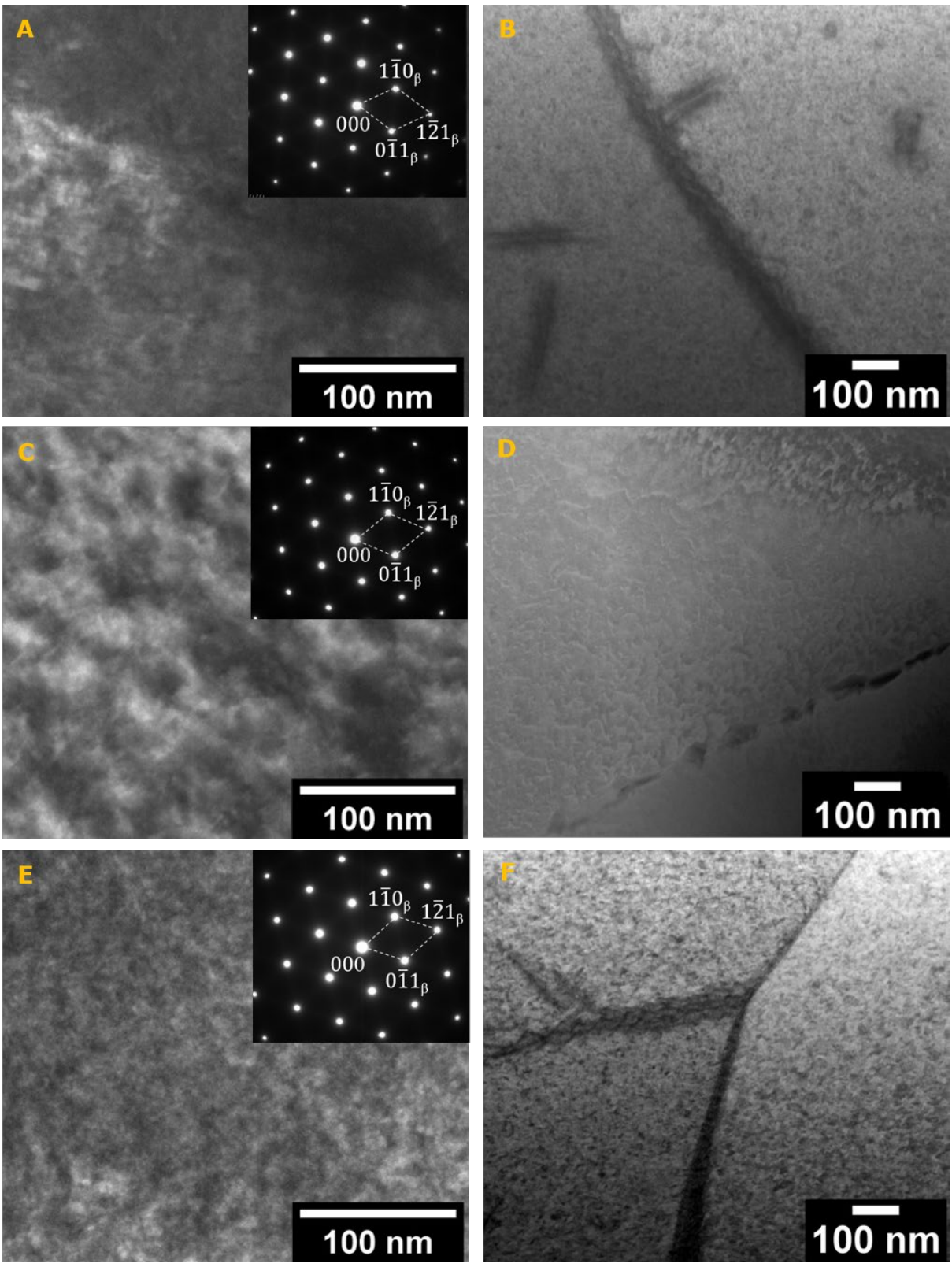

Fig. 9. (A) BF image with corresponding SAD pattern (inset) of as-fabricated TNT alloy, taken from the beta matrix region. (B) BF-STEM image of as-fabricated TNT alloy, taken from a region close to the grain boundary. (C) BF image with corresponding SAD pattern (inset) of as-fabricated TNT5Zr alloy in the beta matrix. (D) BF-STEM image of as-fabricated TNT5Zr alloy, taken from a region close to the grain boundary. (E) BF image with

corresponding SAD pattern (inset) of as-fabricated TNT9Zr alloy in the beta matrix. (F) BF-STEM image of ad-fabricated TNT9Zr alloy, taken from a region close to grain boundary. Note: the beam direction from each capture is parallel to the $[111]_{\beta}$ direction.

3.2 Micro-defects distribution

Fig. 10 demonstrates the reconstructed 3D parts and the quantitative data of defects by the aid of micro-CT technique. Voids (yellow) are with an irregular shape and appear to be randomly distributed in SLM-processed TNT(Z) specimens. The total number of the indexed un-melted particles (red) is smaller than voids in these three alloys. The main difference here is un-melted particles occupy slightly more sites in the TNT5Zr sample than the TNT and TNT9Zr samples. The quantitative data reveals the size of two-type defects is mainly located in the range of 3—20 μm (Fig. 10B). In the histogram, defects size (EqDiameter) here means the equivalent diameter of the spheres with the same volume as the measured defects. The relative density of as-fabricated TNT, TNT5Zr, TNT9Zr samples calculated based on the quantitative data are 99.98%, 99.99% and 99.97%, respectively. Meanwhile, the un-melted particle volume fracture of the TNT, TNT5Zr, TNT9Zr samples calculated based on the quantitative data are 0.0007%, 0.0030% and 0.0020%, respectively.

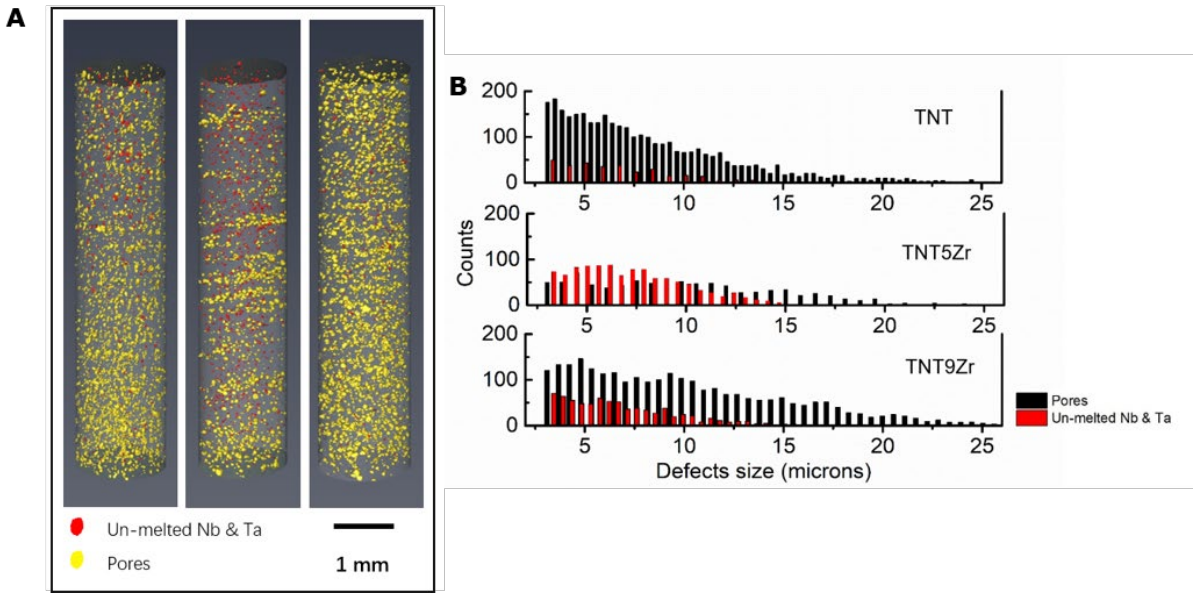

Fig. 10. (A) Un-melted particles and pore defects distribution of as-fabricated TNT (left), TNT5Zr (middle),

TNT9Zr (right) alloy analyzed by micro-CT, and (B) the size and counts of defects inside these samples.

3.3 DSC thermal analysis

High temperature DSC curves of the three TNT(Z) alloys are given in Fig. 11. During the heating process, from room temperature to the upper temperature limit (1200℃), there is an exothermic peak near 678℃ (TNT); the exothermic peaks of the TNT5Zr and TNT9Zr samples are observed near 765℃ and 848℃, respectively. The alpha → beta transus temperature was observed to increase with zirconium addition, and a wide range of no-clear exothermic peak zone was found at the temperature lower than alpha → beta transus. Contrastively, no clear endothermic peaks were observed during the cooling process of the three alloys. According to these curves, the solution treating then water quenching was performed at a temperature (750℃) between the lowest alpha → beta transus temperature (678.6℃) and the highest counterpart temperature (848.3℃).

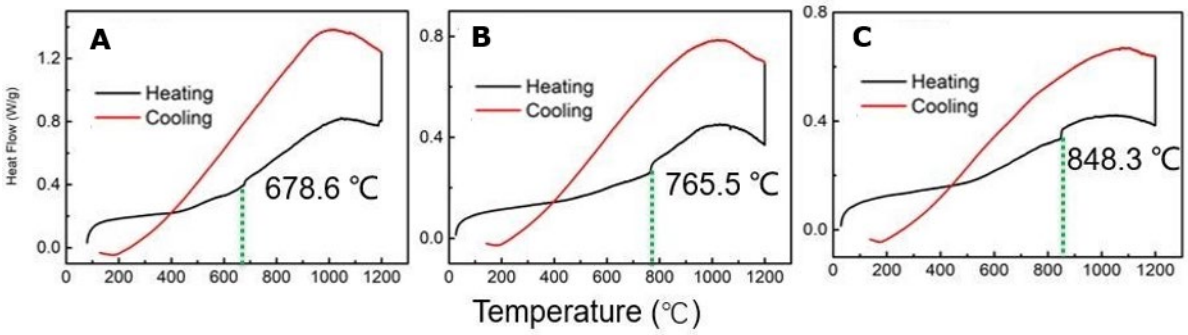

Fig. 11. The DSC heating & cooling curves of (A) TNT, (B) TNT5Zr, and (C) TNT9Zr alloys.

3.4 Vickers hardness and mechanical properties

Fig. 12A reveals Vickers hardness homogeneity of the three alloys from different planes and geometric positions. The micro-hardness of as-fabricated TNT (XOY plane) is 208.5 ± 5.5 HV0.1. The mean value of as-fabricated TNT5Zr (XOY plane) and TNT9Zr (XOY plane) are 232.0 ± 6.5 HV0.1 and 259.7 ± 3.9 HV0.1, respectively. The beta grain refinement made Vickers hardness of TNTZ as-fabricated samples higher than TNT alloy. The material's

microhardness reduction in solution treated condition was observed due to grain growth when dwelling at 750℃ for one hour.

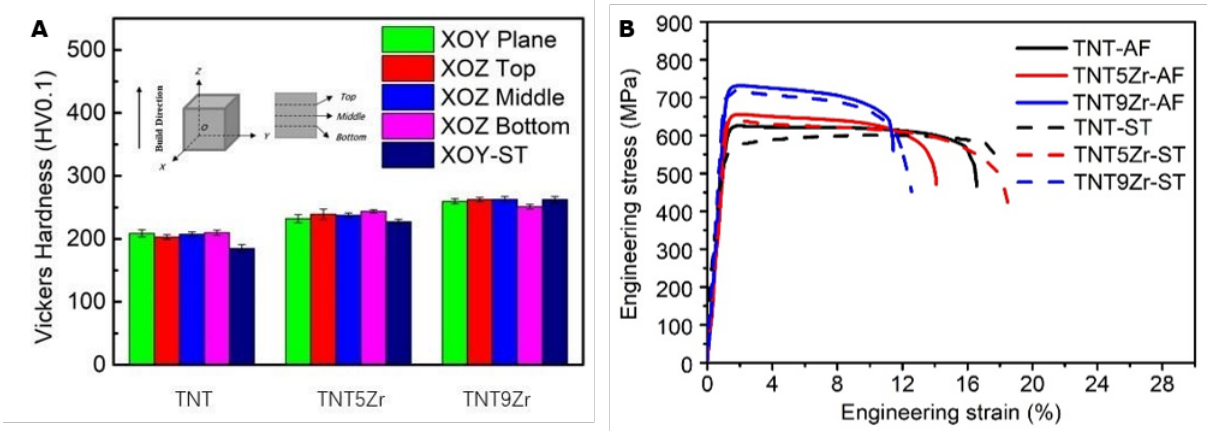

Fig. 12. (A) Vickers hardness of as-fabricated and solution heat treated TNT, TNT5Zr and TNT9Zr alloys, and (B) typical stress-strain curves of these alloys.

Typical stress–strain curves of the as-fabricated and solution-treated TNT, TNT5Zr, TNT9Zr alloys manufactured by SLM are shown in Fig. 12(B). All samples exhibit an ultimate tensile strength (UTS) approx. above 600 MPa and an elongation exceeding 10%. Table 2 demonstrates tensile properties on the three as-mentioned alloys in both conditions. The elastic moduli of as-fabricated TNT(Z) alloys are all less than 70 GPa. Meanwhile, the elongation of as-fabricated TNT(Z) alloys ranges from 11.4% to 14.1%, showing their good ductility. The higher Young's modulus and UTS have been observed after the TNT alloy adding different percentage of zirconium. Meanwhile, the UTS slightly decreases after conducting solution treating then water quenching of these TNT(Z) alloys. Fig. 13A-F reveals typical ductile fractures of these alloys. The large shear-like oval dimple features in as-fabricated TNT specimen are more irregular than the counterpart of as-fabricated TNT5Zr and TNT9Zr. As-fabricated porosity is also found in both conditions of these alloys. The high magnification SEM images show the internal wall of keyhole from the as-fabricated TNT (Fig. 13G) and TNT5Zr alloys (Fig. 13H). It clearly shows the original un-deformed microstructural difference of the two alloys: cellular subgrain (TNT) and equiaxed/columnar mixed grain microstructure (TNT5Zr).

Table 2

Comparison of the tensile properties for the as-fabricated TNT(Z) alloys before and after solution treatment.

Material	E (GPa)	$\sigma_{0.2}$ (MPa)	σ_{UTS} (MPa)	δ (%)	σ_{UTS}/E
TNT-AF	52 ± 3	610 ± 5	681 ± 6	14.1 ± 1.2	12.9 ± 0.6
TNT5Zr-AF	57 ± 5	650 ± 8	698 ± 4	13.7 ± 0.6	12.1 ± 1.1
TNT9Zr-AF	66 ± 5	741 ± 8	772 ± 9	11.4 ± 0.4	11.9 ± 0.8
TNT-ST	47 ± 2	569 ± 2	597 ± 4	15.8 ± 1.8	12.7 ± 0.5
TNT5Zr-ST	56 ± 3	628 ± 3	639 ± 4	16.0 ± 2.6	11.3 ± 0.4
TNT9Zr-ST	66 ± 1	715 ± 2	722 ± 4	14.0 ± 1.4	10.9 ± 0.2

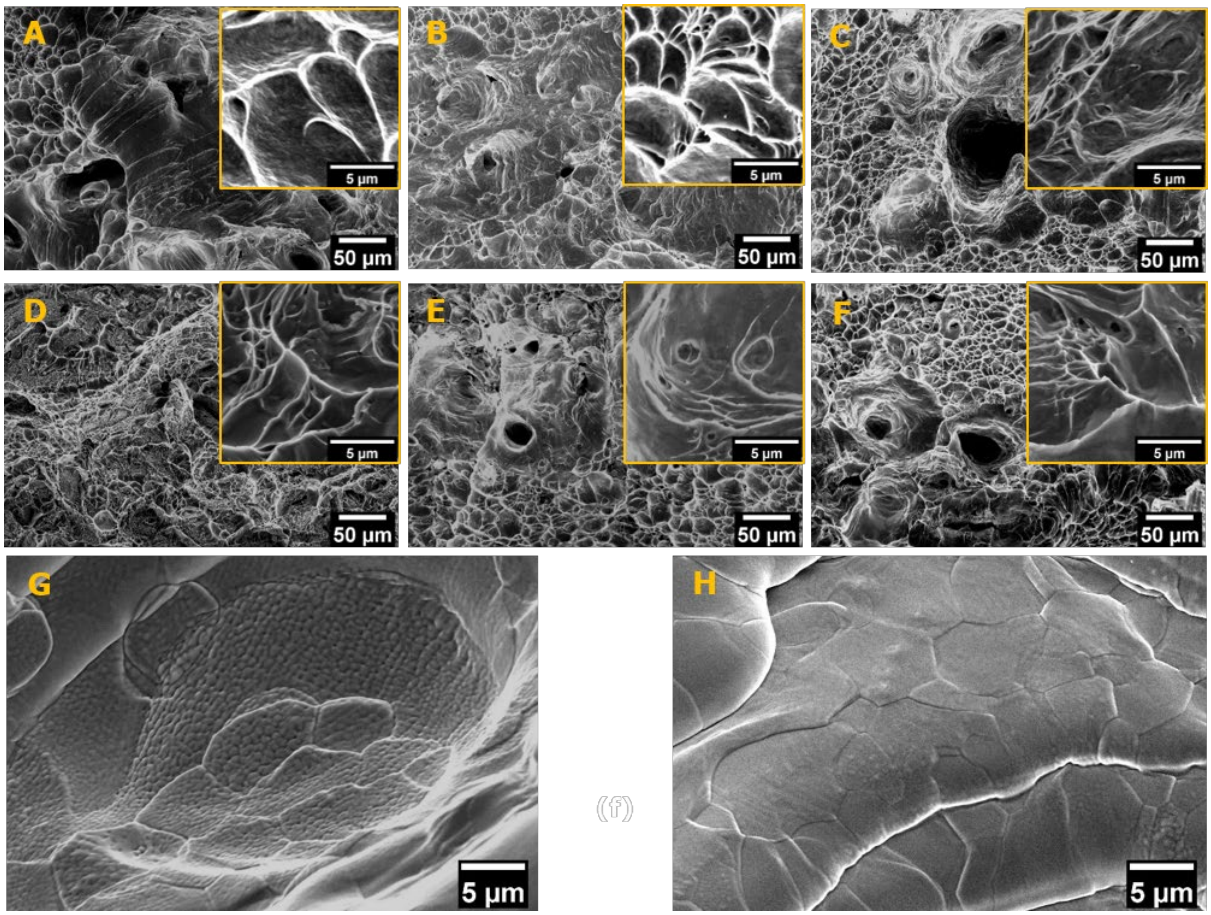

Fig. 13. Tensile fracture morphologies from the (A) as-fabricated TNT, (B) TNT5Zr and (C) TNT9Zr alloys, and (D) solution treated TNT, (E) TNT5Zr and (F) TNT9Zr alloys. (G) The internal wall feature of keyhole from

as-fabricated TNT alloy, and (H) from as-fabricated TNT5Zr alloy.

3.5 Ion release and *in vitro* preosteoblast response

The ion release rate of the three alloys after static immersion testing is shown in Fig. 14. Overall, the concentration of each metallic ion from TNT (Fig. 14A), TNT5Zr (Fig. 14B), TNT9Zr alloys (Fig. 14C) after immersion with MEM containing medium is no more than 10 μg/L. The TNT alloy ion release result seems show a tread that the concentration of the more detectable elements Nb, Ta in the initial stage decrease along with a longer time interval immersion (e.g. 180 days). Conversely, Ti ion concentration appears a slight raise with the growth of immersion time. By comparison, the concentration level of these four metallic ions in TNT5Zr alloy become even lower after Zr addition. Clearly, the mild ion concentration drop from Nb, Ta and no fluctuation from Ti, Zr is found when immersion time increases from 7 to 180 days. Overall, the TNT9Zr alloy ion release result is kept the tread as TNT5Zr alloy. However, a slight Ta ion fluctuation below 5 μg/L is observed in the range of relatively short term immersion (≤30 days). The metabolic activity of MC3T3-E1 preosteoblast cells with the 7, 14, 21, 30, 90 and 180 days released ions and cell culture medium are shown in Fig. 14D. Fairly similar Alamar blue reduction level of each alloy is found after immersion tests at different time intervals when compared to the corresponding control group (Fig. 14D). Noticeably, there happens a decrease in fluorescence of the control group after 180 days immersion by comparison with the other control groups. Osteoblast cells cultured with medium recovered from the ion release assays showcase a prevalence of intact membranes (green) with negligible cells marked as ruptured or damaged (red), see in Fig. 15. Notably, it can't find obvious decrease of cell viability in the culture with metallic ion involved medium when compared to the control ones in each time points form 7 days to 180 days.

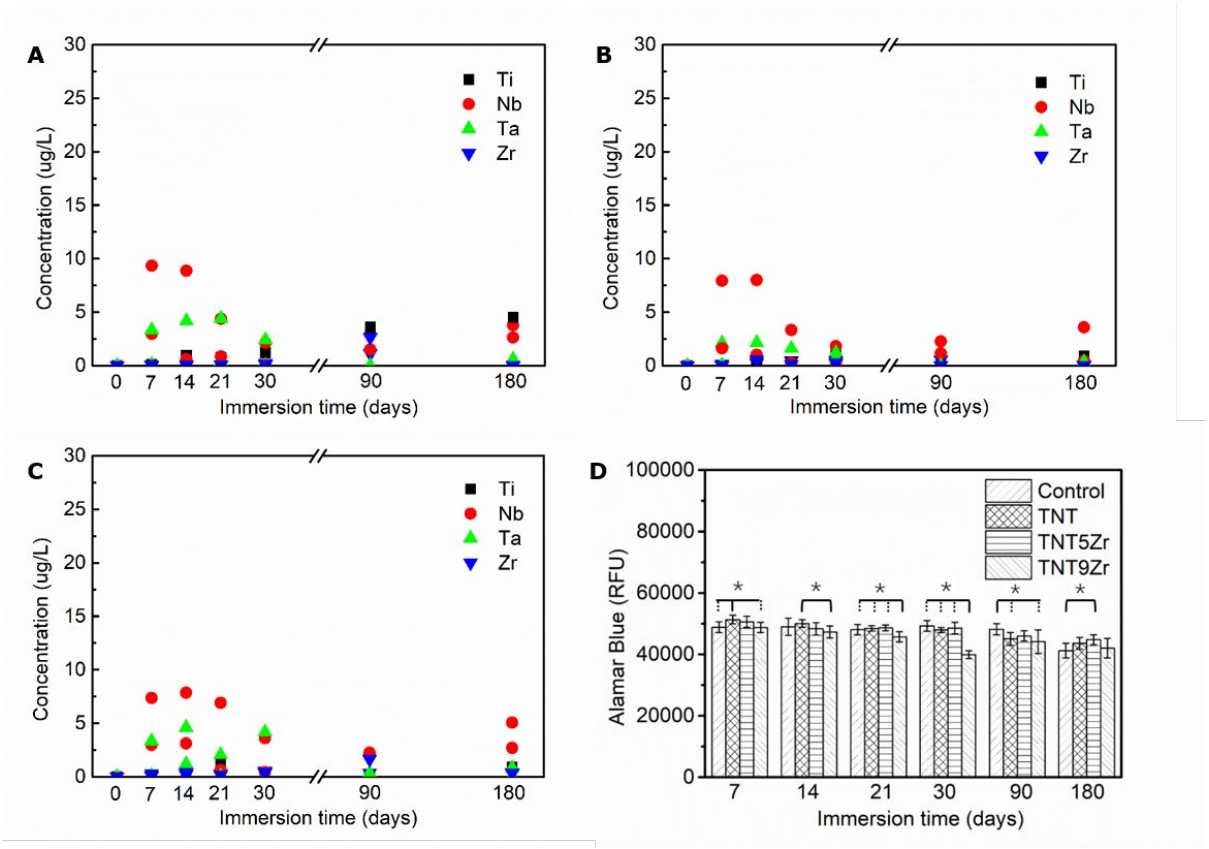

Fig. 14. Ion concentration of the involved elements in (A) TNT, (B) TNT5Zr, and (C) TNT9Zr alloys measured by ICP-OES, and (D) the metabolic activity of MC3T3-E1 preosteoblast cells seeded in after-immersion containing medium, where * signifies *p* value <0.05 (where more than one pair is illustrated, the comparison between the group indicated with a solid line and any other groups indicated with dash lines).

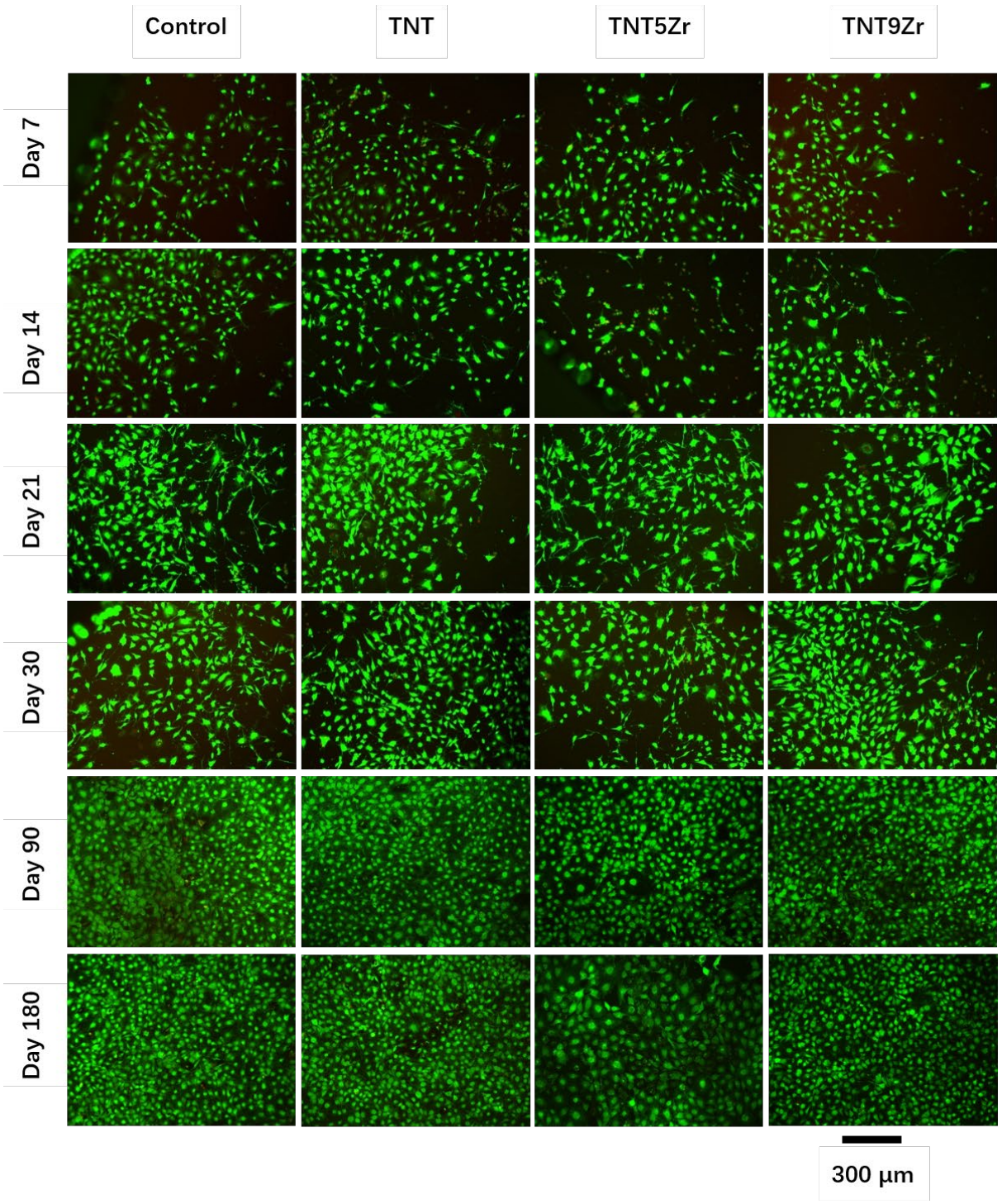

Fig. 15. Micrographs illustrating viability of cells with after-immersion containing medium. Note: live cells are stained in green and dead cells in red.

4. Discussion

4.1 Microstructure evolution and defects distribution

The weak peak (around 35º) found in XRD patterns of the three alloy (Fig. 4), which is suspected to be the peak of alpha phase obtained during rapid cooling upon beta transus temperature in selective laser melting. As the chosen alloys consist of enough beta stabilizers (Nb, Ta), which increases the thermodynamics stability of the β phase in the alloy system. Therefore, martensitic transformation normally induced by high cooling rate is suppressed in these high β-stabilized Ti-Nb-Ta based β alloys, causing the three alloys retain main β phase at room temperature. The same phenomenon that α'' martensite is depressed with the increase of Nb is also reported by Hao et al. [47]. According to the former thermodynamic calculations [48], the classic microstructural evolution e.g. martensitic transformation, diffusionless transformation ($\beta \rightarrow \omega$) will not occur in high Nb composition Ti-Nb alloys during rapid cooling rate processing due to the driving force for the metastable phases nucleation is enough. Additionally, the Zr composition change in alloy chemistry generally produces a shift in the position of the diffraction peaks of the β phase. Zirconium has a calculated atomic radius (206 pm) larger than the replaced element titanium (176 pm) [49], which makes TNT9Zr alloy possess a slightly lower diffraction angle than TNT and TNT5Zr alloys [50]. A large number of grains were statistically analysed in EBSD mapping results (Fig. 5-7), and it found that weak but typical <001> fiber texture was obtained in SLM-processed TNT(Z) alloys. The same preferred crystallographic orientation was also observed in binary Ti-26Nb alloy manufactured by selective laser melting [51] and laser deposited quaternary Ti-34Nb-7Zr-7Ta alloy [52]. The majority of grain growth direction is consistent with main thermal dissipation direction during layer by layer manufacturing in SLM. Also, it appears that the Zr addition induces the grain refinement of TNT5Zr and TNT9Zr alloys manufactured via SLM (Fig. 8A). It may relevant to the occurrence of greater undercooling [53] in melting TNTZ alloys than TNT alloy, which gives rise to more beta grain nucleation sites after Zr element addition. Except for the nucleation rate difference caused by alloying chemistry, short-time high temperature dwell and rapid cooling in the selective laser melting process [54] restrict the growth of nucleated grains. The grain boundary precipitate phases (green) captured by the EBSD phase contrast map are observed in these three alloys. Here, zirconium seems play the role of neutral element in this high β-stabilized Ti-Nb-Ta based alloy because there is no distinguishable precipitate intensity

change when Zr weight percentage increase from 0 to 5%, which is inconsistent with the descriptions as-mentioned before [21,39]. Noticeably, there is a study which attempts to explain the effects of Zr and Sn contents on α'' martensitic transformation of Ti-Nb based β Ti alloys, manufactured by plastically deformed techniques [47]. The conclusions referring to the alloying element effect on microstructural evolution of α'' precipitates should be drawn cautiously due to it may involve stress-induced martensitic transformation on material processing [55].

BF TEM images (Fig. 9A, 9C, 9E) and XRD patterns (Fig. 4) of these as-fabricated TNT(Z) alloys further demonstrate no existence of athermal ω phase inside the beta matrix. These results are inconsistent with the results that nanometer-scale omega and alpha precipitation obtained inside beta matrix from Ti-34Nb-7Zr-7Ta alloy manufactured by direct laser deposition (DLD) [52]; while similar results without precipitation in the beta matrix were found after this as-deposited alloy underwent solution treating then water quenching. We presume metastable precipitate phases probably still can be formed in some beta Ti alloys manufactured by rapid cooling rate processing (e.g. DLD), but they might be suppressed in relative slower cooling rate processing (e.g. quenching, and SLM). The latest microstructure analysis relevant to Ti-35Nb-7Zr-5Ta alloy manufactured by electron beam melting (EBM) reveals the existence of main β phase together with dispersed NbTi4 nanocrystalline intermetallic compound [56]. And these intermetallic precipitates transformed by β phase were also recorded by Li et al. [57] for Ti-10Nb-5Sn alloy heated and cooled repeatedly in the range of room temperature to 400K. Additionally, BF-STEM images of our three alloys show nano-scale grain boundary alpha phase precipitation, which agrees the former EBSD mapping and XRD results. The precipitation starts from beta transus temperature and some embryos nucleate at grain boundary due to the β stabilizer element away from equilibrium in there. However, there is not enough time to grow up properly because the high cooling rate in the SLM process. From the DSC thermal characterization results (Fig. 11) a wide range of no-clear exothermic peak lower than alpha → beta transus temperature was observed. This is consistent with DSC results of Ti-40Nb alloy [58], caused by the lack of athermal omega phase decomposition during heat up in these alloys. Meanwhile, no measurable sharp exothermic peak was observed during the slow furnace cooling process, probably because the material undergoes smooth alpha phase growth

along grain boundary [59].

Micro-CT provides a feasible characterization thread to quantify the SLM-processed defects. The results in Fig. 10 show the high relative density (≥99.97%) and extremely small amount of un-melted Nb & Ta particles of SLM-processed TNT(Z) specimens. The void shape tends to be irregular, which is regarded as the keyhole. The mechanism of its formation is due to local evaporation of the lowest boiling point element titanium when perform high-speed *in-situ* alloying by SLM, which appears similar to the findings from Liu et al. [37]. Meanwhile, the rocky pure powders (like Nb, Ta) may increase the difficulty of evenly spreading the powder bed. Hence, the localized evaporation probably happens somewhere with a smaller amount of refractory element powder existence. The un-melted particles inside these SLM-processed materials may happen when performing *in-situ* alloying on the zones with relatively coarser refractory powder, the laser incident energy from scanning and remelting cannot thoroughly melt these particles. This is common found when *in-situ* alloying pure elements with different thermal physical properties [60], but the percentage of un-melted particles can be minor after a systematic parameter optimization.

4.2 Micro-hardness and tensile properties

There appears a small variation of as-measured Vickers hardness values (Fig. 12A) in different positions of the as-fabricated TNT(Z) specimens, which positively demonstrates that no obvious macro-structure inhomogeneity exists via *in-situ* alloying TNT(Z) alloys. The low Vickers hardness value (203-264 HV0.1) obtained here is at the same level of SLMed Ti-24Nb-4Zr-8Sn alloy, with a high relative density (>99%) [36]. This is mainly because of low critical resolved shear stress when slip happens in these body-centered cubic (bcc) β Ti alloys. From stress-strain curves of as-fabricated TNT(Z) specimens (Fig. 12B), ultimate tensile strength (UTS) of these as-fabricated β Ti alloys is at the range from 681 ± 6 MPa to 772 ± 9 MPa. As-fabricated TNT alloy obtained the lowest UTS (681 ± 6 MPa), staying at the same UTS level of additive manufactured Ti-30Nb-5Ta-3Zr alloy [61] and Ti-24Nb-4Zr-8Sn alloy [36]. By comparing to cold rolling + solution treating then quenching beta alloys with enough β stabilizers, like Ti-35%Nb-4%Sn or Ti-35%Nb-7.9%Sn (approx. 500 MPa in UTS) [62], grain

size difference is regarded as the main factor to decide why there exists a UTS gap. Beta grain size refinement in AM-processed TNT(Z) alloys happens mainly due to its rapid solidification from high temperature. Contrastively, beta grain of the aforementioned Ti-Nb-Sn alloys manufactured by traditional techniques undergo a thorough growth when the long-time dwell above beta transus during solution treatment.

The UTS to modulus ratio is a crucial value to evaluate the mechanical stability of orthopedic implants. In this work, all three alloys obtained a high strength-to-modulus ratio of approx. 12 (see in table 2), while the recorded value of biomedical Ti-6Al-4V alloy was reported to variate between 8.1-8.8 [63]. To explain the UTS increase after zirconium additions in TNTZ alloys found in table 2, as dislocations in one crystal pile up on the grain boundary, leading to a high stress concentration in the boundary and neighboring grains. Hence, higher level grain refinement material (TNT9Zr alloy) provides more grain boundary barriers, thus making this material the strongest [64]. Besides that, UTS, Young's modulus, and Vickers hardness experienced a weak reduction after solution treating then water quenching. This can be regarded as the grain growth after performing a dwell at solution treated temperature, and no extra metastable precipitates form during water quenching process. After comparison with the fracture morphologies (Fig. 13(A-F)) of different alloys at both as-fabricated and solution treated conditions, these specimens all undergo dimple rupture with relatively high ductility (>10%). There exists nucleation, growth and coalescence of microvoids at grain boundary, and fracture happens after an accumulation of critical local strain for microvoids [65]. In particular, the shear-like oval dimples obtained from as-fabricated TNT(Z) alloys turn into more regular equiaxed dimples (Fig. 13(D-F)) after conducting solution treating then water quenching. The common found dimple shape appears after materials' solution treatment probably relevant to the grain growth and reorientation. Fig. 13G-H presents the virgin microstructure of as-fabricated TNT and TNT5Zr alloy; the cellular subgrains inside the equiaxed beta grain structure are observed inside un-deformed pores of as-fabricated TNT alloy. The smaller amounts of undercooling during TNT alloy solidification promote the formation of cellular subgrains. It has been observed that the misorientation angle between subgrains is around 1-2º [66], which seems explain why as-fabricated TNT alloy obtains the highest percentage of low misorientation angle (≤5º) in these three alloys.

4.3 Ion release and biocompatibility evaluation

This study has evaluated long-term ion release rate for the three defined alloys submerged in MEM containing medium and *in vitro* preosteoblast response to after-immersion medium. Ion release results (Fig. 14(A-C)) confirm that these investigated alloys possess good corrosion resistance because the highest metallic ion concentration is extremely small (<10 μg/L). The corrosion ions origin from uniform attack contain a higher concentration in the first 14 days immersion than the other time interval immersion. It is assumed that the acid salts (e.g. $MgCl_2$, $CaCl_2$, etc.) from MEM containing medium generate a relatively higher extent of corrosion products when reacting with each alloy in the first stage (≤ 14 days). The corrosion product film on these TNT(Z) alloys becomes fairly stable after 30 days immersion, potentially further slowing down the overall corrosion rate. It indicated that good biocompatibility with respect to cytotoxicity during culture with corrosion ions is obtained in these TNT(Z) alloys. As the overall metallic ion concentration is small, no obvious cytotoxicity can be found after cell culture even though the highest time interval is 6 month. The same positive results can be found in short-term (maximum 4 weeks) titanium, niobium, and tantalum wire implantation in soft and hard bone rat tissue [67]. No dissolution of Ti, Nb, Ta was detected in peri-implant tissues and no inflammatory response was observed around these implants. The literature [68] demonstrates that proteins in an *in vivo* environment can interplay with the corrosion reactions of metallic implants in several ways: proteins bind to metal ions and transport them away from the solid-liquid interface, thus accelerating further ion dissolution; the proteins may adhere to the alloy surface and restrict the diffusion of oxygen to the surface, potentially blocking the metal surface re-passivation. However, it is difficult to mimic a serum containing cell culture *in vitro* environment for 30 days ion release evaluation due to its short shelf life when incubated in a 37 °C atmosphere. Meanwhile, it should be noted that the quantification of released metallic ions from these three alloys is also challenging. The excellent corrosion resistant TNT(Z) alloys extract small concentration ions in MEM containing medium. If analyzed using higher resolution facility (e.g. ICP-MS), proper dilution is needed due to high concentration background Ca^{2+} in MEM medium. However, the liquid samples should be a high percentage

below the detection limit after that operation. Though the ion release rate can be increased by using strong acid or another corrosive medium, the chance to combine ion release test and cytotoxicity assays together will be lost.

5. Conclusions

This study investigated *in-situ* alloying Ti-Nb-Ta based β alloys with different zirconium additions (0, 5, 9 wt. %) manufactured by selective laser melting (SLM) for load-bearing implant development. The microstructure and defects, mechanical properties, and biocompatibility were systematically analyzed, and the following main conclusions are drawn:

1. The slow scan speed (e.g. 500 mm/s) with high laser power (e.g. 300 W) is accepted as being an optional parameter combination to manufacture TNT(Z) alloys at a low defects level. Micro-CT results show that the size of un-melted particles (Nb & Ta) and keyhole of after-optimization TNT(Z) alloys is mainly located in a range of 3—20 μm, and the relative density of as-fabricated TNT(Z) alloys is >99.97%.
2. Martensitic transformation normally caused by high cooling is suppressed in the high β-stabilized Ti-Nb-Ta based alloys, making these three as-SLMed alloys obtain main β phase at room temperature. No existence of athermal ω or α'' phase inside the beta matrix and potential nano-scale grain boundary alpha phase precipitation is observed in TNT(Z) alloys, which agrees the relevant EBSD mapping and XRD results. Additionally, zirconium is regarded as a neutral element in this high β-stabilized Ti-Nb-Ta based alloy when perform SLM manufacturing.
3. Tensile testing shows that the ultimate tensile strength (UTS) of these as-fabricated β Ti alloys ranges from 681 ± 6 MPa to 772 ± 9 MPa. Here, the Vickers hardness and UTS increase caused by zirconium addition is explained by grain refinement. A weak UTS reduction after solution treating then water quenching is regarded as grain growth when dwell at solution treated temperature. Notably, the UTS to modulus ratio of as-designed TNT(Z) alloys is approx. 12, which is much higher than the recorded value (8.1-8.8) of biomedical Ti-6Al-4V alloy.

4. Corrosion ions released from uniform attack in MEM containing medium at each time interval have an extremely small concentration (<10 μg/L). The corrosion product film on these TNT(Z) alloys, presumably to be fairly stable after 30 days immersion. It indicated that good biocompatibility with respect to cytotoxicity during culture with corrosion ions is obtained in these TNT(Z) alloys.

Declaration of Competing Interest

The authors declare no conflicts of interest directly relevant to the work reported in this paper.

Acknowledgement

WK acknowledges the financial support for the TEM characterization work provided by Institute of New Materials, Guangdong Academy of Science (PI: MMA, grant: 17-0551), as well as the chemical analysis from School of Geography, Earth and Environmental Sciences, University of Birmingham.

References

[1] A.D. Woolf, B. Pfleger, Burden of major musculoskeletal conditions, Bull. World Health Organ. (2003). https://doi.org/10.1590/S0042-96862003000900007.

[2] D.J. Hunter, S. Bierma-Zeinstra, Osteoarthritis, Lancet. (2019). https://doi.org/10.1016/S0140-6736(19)30417-9.

[3] Q. Chen, G.A. Thouas, Metallic implant biomaterials, Mater. Sci. Eng. R Reports. (2015). https://doi.org/10.1016/j.mser.2014.10.001.

[4] T.M. Sridhar, S.P. Vinodhini, U. Kamachi Mudali, B. Venkatachalapathy, K. Ravichandran, Load-bearing metallic implants: electrochemical characterisation of corrosion phenomena, Mater. Technol. (2016). https://doi.org/10.1080/10667857.2016.1220752.

[5] M. Fousová, D. Vojtěch, J. Kubásek, E. Jablonská, J. Fojt, Promising characteristics of gradient porosity Ti-6Al-4V alloy prepared by SLM process, J. Mech. Behav. Biomed. Mater. (2017). https://doi.org/10.1016/j.jmbbm.2017.01.043.

[6] P.K. Zysset, X. Edward Guo, C. Edward Hoffler, K.E. Moore, S.A. Goldstein, Elastic modulus and hardness of cortical and trabecular bone lamellae measured by nanoindentation in the human femur, J. Biomech. (1999). https://doi.org/10.1016/S0021-9290(99)00111-6.

[7] R. HUISKES, H. WEINANS, B. VAN RIETBERGEN, The Relationship Between Stress Shielding and Bone Resorption Around Total Hip Stems and the Effects of Flexible Materials, Clin. Orthop. Relat. Res. (1992). https://doi.org/10.1097/00003086-

199201000-00014.
[8] J.P. Paul, Strength requirements for internal and external prostheses, J. Biomech. (1999). https://doi.org/10.1016/S0021-9290(98)00190-0.
[9] W.D. Bugbee, W.J. Culpepper, C. a Engh, Long-term clinical consequences of stress-shielding after total hip arthroplasty without cement., J. Bone Joint Surg. Am. (1997).
[10] J.D. BOBYN, E.S. MORTIMER, A.H. GLASSMAN, C.A. ENGH, J.E. MILLER, C.E. BROOKS, Producing and Avoiding Stress Shielding, Clin. Orthop. Relat. Res. (1992). https://doi.org/10.1097/00003086-199201000-00010.
[11] D. Kuroda, M. Niinomi, M. Morinaga, Y. Kato, T. Yashiro, Design and mechanical properties of new β type titanium alloys for implant materials, Mater. Sci. Eng. A. (1998). https://doi.org/10.1016/s0921-5093(97)00808-3.
[12] S. Amin Yavari, R. Wauthle, J. Van Der Stok, A.C. Riemslag, M. Janssen, M. Mulier, J.P. Kruth, J. Schrooten, H. Weinans, A.A. Zadpoor, Fatigue behavior of porous biomaterials manufactured using selective laser melting, Mater. Sci. Eng. C. (2013). https://doi.org/10.1016/j.msec.2013.08.006.
[13] B. Van Hooreweder, Y. Apers, K. Lietaert, J.P. Kruth, Improving the fatigue performance of porous metallic biomaterials produced by Selective Laser Melting, Acta Biomater. (2017). https://doi.org/10.1016/j.actbio.2016.10.005.
[14] S. Catalani, S. Stea, A. Beraudi, M.E. Gilberti, B. Bordini, A. Toni, P. Apostoli, Vanadium release in whole blood, serum and urine of patients implanted with a titanium alloy hip prosthesis, Clin. Toxicol. (2013). https://doi.org/10.3109/15563650.2013.818682.
[15] P.J. Bania, Beta titanium alloys and their role in the titanium industry, JOM. (1994). https://doi.org/10.1007/BF03220742.
[16] R. Banerjee, S. Nag, J. Stechschulte, H.L. Fraser, Strengthening mechanisms in Ti-Nb-Zr-Ta and Ti-Mo-Zr-Fe orthopaedic alloys, Biomaterials. (2004). https://doi.org/10.1016/j.biomaterials.2003.10.041.
[17] Y. Al-Zain, H.Y. Kim, H. Hosoda, T.H. Nam, S. Miyazaki, Shape memory properties of Ti-Nb-Mo biomedical alloys, Acta Mater. (2010). https://doi.org/10.1016/j.actamat.2010.04.013.
[18] W.T. Huo, L.Z. Zhao, S. Yu, Z.T. Yu, P.X. Zhang, Y.S. Zhang, Significantly enhanced osteoblast response to nano-grained pure tantalum, Sci. Rep. (2017). https://doi.org/10.1038/srep40868.
[19] L. Trentani, F. Pelillo, F.C. Pavesi, L. Ceciliani, G. Cetta, A. Forlino, Evaluation of the TiMo12Zr6Fe2 alloy for orthopaedic implants: In vitro biocompatibility study by using primary human fibroblasts and osteoblasts, Biomaterials. (2002). https://doi.org/10.1016/S0142-9612(01)00413-6.
[20] M. Morinaga, Alloy design based on molecular orbital method, Mater. Trans. (2016). https://doi.org/10.2320/matertrans.M2015418.
[21] M. Abdel-Hady, K. Hinoshita, M. Morinaga, General approach to phase stability and elastic properties of β-type Ti-alloys using electronic parameters, Scr. Mater. (2006). https://doi.org/10.1016/j.scriptamat.2006.04.022.
[22] N. Sakaguchi, M. Niinomi, T. Akahori, J. Takeda, H. Toda, Relationships between tensile deformation behavior and microstructure in Ti-Nb-Ta-Zr system alloys, in: Mater.

Sci. Eng. C, 2005. https://doi.org/10.1016/j.msec.2004.12.014.
[23] Y.S. Zhukova, Y.A. Pustov, A.S. Konopatsky, S.M. Dubinskiy, M.R. Filonov, V. Brailovski, Corrosion fatigue and electrochemical behavior of superelastic Ti-Nb-Ta alloy for medical implants under cyclic load conditions, Mater. Today Proc. (2015). https://doi.org/10.1016/j.matpr.2015.07.448.
[24] D.M. Gordin, R. Ion, C. Vasilescu, S.I. Drob, A. Cimpean, T. Gloriant, Potentiality of the "gum Metal" titanium-based alloy for biomedical applications, Mater. Sci. Eng. C. (2014). https://doi.org/10.1016/j.msec.2014.08.003.
[25] P. Neacsu, D.M. Gordin, V. Mitran, T. Gloriant, M. Costache, A. Cimpean, In vitro performance assessment of new beta Ti-Mo-Nb alloy compositions, Mater. Sci. Eng. C. (2015). https://doi.org/10.1016/j.msec.2014.11.023.
[26] A. Basak, S. Das, Epitaxy and Microstructure Evolution in Metal Additive Manufacturing, Annu. Rev. Mater. Res. (2016). https://doi.org/10.1146/annurev-matsci-070115-031728.
[27] D.L. Bourell, Perspectives on Additive Manufacturing, Annu. Rev. Mater. Res. (2016). https://doi.org/10.1146/annurev-matsci-070115-031606.
[28] L.E. Murr, S.M. Gaytan, D.A. Ramirez, E. Martinez, J. Hernandez, K.N. Amato, P.W. Shindo, F.R. Medina, R.B. Wicker, Metal Fabrication by Additive Manufacturing Using Laser and Electron Beam Melting Technologies, J. Mater. Sci. Technol. (2012). https://doi.org/10.1016/S1005-0302(12)60016-4.
[29] S.H. Huang, P. Liu, A. Mokasdar, L. Hou, Additive manufacturing and its societal impact: A literature review, Int. J. Adv. Manuf. Technol. (2013). https://doi.org/10.1007/s00170-012-4558-5.
[30] C. Körner, Additive manufacturing of metallic components by selective electron beam melting - A review, Int. Mater. Rev. (2016). https://doi.org/10.1080/09506608.2016.1176289.
[31] S. Wu, X. Liu, K.W.K. Yeung, C. Liu, X. Yang, Biomimetic porous scaffolds for bone tissue engineering, Mater. Sci. Eng. R Reports. (2014). https://doi.org/10.1016/j.mser.2014.04.001.
[32] S.C. Cox, P. Jamshidi, N.M. Eisenstein, M.A. Webber, H. Hassanin, M.M. Attallah, D.E.T. Shepherd, O. Addison, L.M. Grover, Adding functionality with additive manufacturing: Fabrication of titanium-based antibiotic eluting implants, Mater. Sci. Eng. C. (2016). https://doi.org/10.1016/j.msec.2016.04.006.
[33] H. Hassanin, L. Finet, S.C. Cox, P. Jamshidi, L.M. Grover, D.E.T. Shepherd, O. Addison, M.M. Attallah, Tailoring selective laser melting process for titanium drug-delivering implants with releasing micro-channels, Addit. Manuf. (2018). https://doi.org/10.1016/j.addma.2018.01.005.
[34] H.E. Burton, N.M. Eisenstein, B.M. Lawless, P. Jamshidi, M.A. Segarra, O. Addison, D.E.T. Shepherd, M.M. Attallah, L.M. Grover, S.C. Cox, The design of additively manufactured lattices to increase the functionality of medical implants, Mater. Sci. Eng. C. (2019). https://doi.org/10.1016/j.msec.2018.10.052.
[35] T.A. Schaedler, W.B. Carter, Architected Cellular Materials, Annu. Rev. Mater. Res. (2016). https://doi.org/10.1146/annurev-matsci-070115-031624.
[36] L.C. Zhang, D. Klemm, J. Eckert, Y.L. Hao, T.B. Sercombe, Manufacture by selective

laser melting and mechanical behavior of a biomedical Ti-24Nb-4Zr-8Sn alloy, Scr. Mater. (2011). https://doi.org/10.1016/j.scriptamat.2011.03.024.
[37] Y.J. Liu, S.J. Li, H.L. Wang, W.T. Hou, Y.L. Hao, R. Yang, T.B. Sercombe, L.C. Zhang, Microstructure, defects and mechanical behavior of beta-type titanium porous structures manufactured by electron beam melting and selective laser melting, Acta Mater. (2016). https://doi.org/10.1016/j.actamat.2016.04.029.
[38] G. Lütjering, J.C. Williams, Titanium : Engineering Materials and Processes, 2007. https://doi.org/10.1007/978-3-540-73036-1.
[39] Y.L. Hao, S.J. Li, F. Prima, R. Yang, Controlling reversible martensitic transformation in titanium alloys with high strength and low elastic modulus, Scr. Mater. (2012). https://doi.org/10.1016/j.scriptamat.2012.06.011.
[40] C.Y. Yap, C.K. Chua, Z.L. Dong, Z.H. Liu, D.Q. Zhang, L.E. Loh, S.L. Sing, Review of selective laser melting: Materials and applications, Appl. Phys. Rev. (2015). https://doi.org/10.1063/1.4935926.
[41] ASTM E8, ASTM E8/E8M standard test methods for tension testing of metallic materials 1, Annu. B. ASTM Stand. 4. (2010). https://doi.org/10.1520/E0008.
[42] E384-17, Standard Test Method for Microindentation Hardness of Materials, ASTM B. Stand. (2017). https://doi.org/10.1520/E0384-17.
[43] A. International, Standard Guide for Quantitating Cell Viability Within Biomaterial Scaffolds 1, Annu. B. ASTM Stand. (2011). https://doi.org/10.1520/F2739-08.2.
[44] T. Mukherjee, J.S. Zuback, A. De, T. DebRoy, Printability of alloys for additive manufacturing, Sci. Rep. (2016). https://doi.org/10.1038/srep19717.
[45] K. Darvish, Z.W. Chen, T. Pasang, Reducing lack of fusion during selective laser melting of CoCrMo alloy: Effect of laser power on geometrical features of tracks, Mater. Des. (2016). https://doi.org/10.1016/j.matdes.2016.09.086.
[46] A. Matsunawa, J.-D. Kim, N. Seto, M. Mizutani, S. Katayama, Dynamics of keyhole and molten pool in laser welding, J. Laser Appl. (1998). https://doi.org/10.2351/1.521858.
[47] Y.L. Hao, S.J. Li, S.Y. Sun, R. Yang, Effect of Zr and Sn on Young's modulus and superelasticity of Ti-Nb-based alloys, Mater. Sci. Eng. A. (2006). https://doi.org/10.1016/j.msea.2006.09.051.
[48] Y. Zhang, H. Liu, Z. Jin, Thermodynamic assessment of the Nb-Ti system, Calphad Comput. Coupling Phase Diagrams Thermochem. (2001). https://doi.org/10.1016/S0364-5916(01)00051-7.
[49] E. Clementi, D.L. Raimondi, W.P. Reinhardt, Atomic screening constants from SCF functions. II. Atoms with 37 to 86 electrons, J. Chem. Phys. (1967). https://doi.org/10.1063/1.1712084.
[50] D.L. Dorset, X-ray Diffraction: A Practical Approach, Microsc. Microanal. (1998). https://doi.org/10.1017/S143192769800049X.
[51] M. Fischer, D. Joguet, G. Robin, L. Peltier, P. Laheurte, In situ elaboration of a binary Ti-26Nb alloy by selective laser melting of elemental titanium and niobium mixed powders, Mater. Sci. Eng. C. (2016). https://doi.org/10.1016/j.msec.2016.02.033.
[52] S. Nagn, R. Banerjee, Laser deposition and deformation behavior of Ti-Nb-Zr-Ta alloys for orthopedic implan, J. Mech. Behav. Biomed. Mater. (2012).

https://doi.org/10.1016/j.jmbbm.2012.08.014.
[53] H. Men, Z. Fan, Effects of solute content on grain refinement in an isothermal melt, Acta Mater. (2011). https://doi.org/10.1016/j.actamat.2011.01.008.
[54] S.L. Sing, J. An, W.Y. Yeong, F.E. Wiria, Laser and electron-beam powder-bed additive manufacturing of metallic implants: A review on processes, materials and designs, J. Orthop. Res. (2016). https://doi.org/10.1002/jor.23075.
[55] Y.L. Hao, S.J. Li, S.Y. Sun, C.Y. Zheng, R. Yang, Elastic deformation behaviour of Ti-24Nb-4Zr-7.9Sn for biomedical applications, Acta Biomater. (2007). https://doi.org/10.1016/j.actbio.2006.11.002.
[56] M. Surmeneva, I. Grubova, N. Glukhova, D. Khrapov, A. Koptyug, A. Volkova, Y. Ivanov, C.M. Cotrut, A. Vladescu, A. Teresov, N. Koval, A. Tyurin, R. Surmenev, New ti–35nb–7zr–5ta alloy manufacturing by electron beam melting for medical application followed by high current pulsed electron beam treatment, Metals (Basel). (2021). https://doi.org/10.3390/met11071066.
[57] Y. Li, J. Qi, R. Fan, C. Zhai, C. Xu, In-situ TEM observation of phase transformation for bio-medical shape memory TiNbSn alloy, in: Adv. Mater. Res., 2011. https://doi.org/10.4028/www.scientific.net/AMR.152-153.1755.
[58] Y. Mantani, M. Tajima, Phase transformation of quenched α″ martensite by aging in Ti-Nb alloys, Mater. Sci. Eng. A. (2006). https://doi.org/10.1016/j.msea.2006.02.180.
[59] S. Nag, R. Banerjee, H.L. Fraser, Microstructural evolution and strengthening mechanisms in Ti-Nb-Zr-Ta, Ti-Mo-Zr-Fe and Ti-15Mo biocompatible alloys, in: Mater. Sci. Eng. C, 2005. https://doi.org/10.1016/j.msec.2004.12.013.
[60] J.C. Wang, Y.J. Liu, P. Qin, S.X. Liang, T.B. Sercombe, L.C. Zhang, Selective laser melting of Ti–35Nb composite from elemental powder mixture: Microstructure, mechanical behavior and corrosion behavior, Mater. Sci. Eng. A. (2019). https://doi.org/10.1016/j.msea.2019.06.001.
[61] J.P. Luo, J.F. Sun, Y.J. Huang, J.H. Zhang, D.P. Zhao, M. Yan, Y.D. Zhang, Low-modulus biomedical Ti–30Nb–5Ta–3Zr additively manufactured by Selective Laser Melting and its biocompatibility, Mater. Sci. Eng. C. (2019). https://doi.org/10.1016/j.msec.2018.11.077.
[62] S. Hanada, H. Matsumoto, S. Watanabe, Mechanical compatibility of titanium implants in hard tissues, Int. Congr. Ser. (2005). https://doi.org/10.1016/j.ics.2005.06.084.
[63] M. Niinomi, Mechanical properties of biomedical titanium alloys, Mater. Sci. Eng. A. (1998). https://doi.org/10.1016/s0921-5093(97)00806-x.
[64] L. Priester, Grain Boundaries: From Theory to Engineering, 2013. https://doi.org/10.1007/978-94-007-4969-6.
[65] J.C. Williams, B.S. Hickman, H.L. Marcus, The effect of omega phase on the mechanical properties of titanium alloys, Metall. Trans. (1971). https://doi.org/10.1007/BF02913423.
[66] Y.M. Wang, T. Voisin, J.T. McKeown, J. Ye, N.P. Calta, Z. Li, Z. Zeng, Y. Zhang, W. Chen, T.T. Roehling, R.T. Ott, M.K. Santala, P.J. Depond, M.J. Matthews, A. V. Hamza, T. Zhu, Additively manufactured hierarchical stainless steels with high strength and ductility, Nat. Mater. (2018). https://doi.org/10.1038/NMAT5021.
[67] H. Matsuno, A. Yokoyama, F. Watari, M. Uo, T. Kawasaki, Biocompatibility and

osteogenesis of refractory metal implants, titanium, hafnium, niobium, tantalum and rhenium, Biomaterials. (2001). https://doi.org/10.1016/S0142-9612(00)00275-1.

[68] M.A. Khan, R.L. Williams, D.F. Williams, The corrosion behaviour of Ti-6Al-4V, Ti-6Al-7Nb and Ti-13Nb-13Zr in protein solutions, Biomaterials. (1999). https://doi.org/10.1016/S0142-9612(98)00217-8.